John von Neumann Institute for Computing

Liquid Crystal Systems

Michael P. Allen

published in

Computational Soft Matter: From Synthetic Polymers to Proteins, Lecture Notes,
Norbert Attig, Kurt Binder, Helmut Grubmüller, Kurt Kremer (Eds.),
John von Neumann Institute for Computing, Jülich,
NIC Series, Vol. **23***, ISBN 3-00-012641-4, pp. 289-320, 2004.*

http://www.fz-juelich.de/nic-series/volume23

Liquid Crystal Systems

Michael P. Allen

Centre for Scientific Computing and Department of Physics,
University of Warwick, Coventry CV4 7AL, United Kingdom
E-mail: m.p.allen@warwick.ac.uk

This chapter gives an overview of Monte Carlo and molecular dynamics simulations of liquid crystals. Over the last fifteen years, most effort has focused on the development of methods for measuring, by simulation, the essential defining properties of liquid crystals: the phase behaviour, elastic constants, and surface anchoring coefficients. For this purpose, simple molecular models which reflect the essential physics are sufficient. The results of these simulations are frequently compared with theoretical predictions based on Oseen-Frank orientational elasticity, the Landau-de Gennes free energy, or density functionals. More recently, simulations using simple models have been extended to systems involving colloids and defects. Some references will also be made to the development of simulations using more realistic molecular models, which allow comparison with experiment.

1 Introduction

The computer simulation of liquid crystals is a rapidly expanding field: many of the techniques needed to measure the properties of interest, and to study the relevant phase transitions, are still being developed. In principle, computer simulation combined with liquid-state theories should give us an insight into the link between molecular structure and liquid crystalline behaviour. In practice, this approach complements the very well established experimental method of synthesizing and testing large numbers of compounds. The sensitivity of liquid crystal properties to molecular details means that simulation faces a tough challenge. Nonetheless, the first elements of a coherent picture are beginning to emerge from simulations, and the prospects look good for further progress. Onsager's theory is an early example of the now-popular density-functional theories of the liquid state: such theories directly link molecular properties with bulk-phase behaviour. Computer simulation can make a valuable contribution by testing theories of this kind, perhaps pointing the way to improving them. The first part of this chapter gives examples of this kind of study.

Continuum models of liquid crystals, based on phenomenological elastic constants and hydrodynamic transport coefficients, have been outstandingly successful in modelling behaviour on the length and time scales of most interest to device manufacturers. Simulation can contribute by providing methods of calculating the relevant coefficients for a given molecular model. Moreover, interest is developing in molecular-scale effects, such as behaviour near surfaces and defects, which cannot be modelled properly in the continuum picture. To bridge the gap, it is necessary to simulate very large systems, and some recent work in this area will be described in the second part of this chapter.

2 Molecular Models

Liquid crystals may be modelled at various levels of detail. Atomistic simulations, based on empirical potentials[1,2] and/or *ab initio* calculations[3–5], are intended to calculate the

properties of specific molecular systems, but current computer power limits the sample sizes to a few thousand molecules with simulation times up to a few tens of nanoseconds. By using more coarse-grained models, in which the molecule is represented by a single non-spherical unit, these figures may be extended by an order of magnitude or more, at the cost of blurring the connection between molecular structure and liquid crystalline properties. Liquid crystalline properties and phase behaviour are extremely sensitive to details of molecular structure and interactions, so it is a great challenge for either simulation or theory to contribute to the design and synthesis of new materials. Moreover, interest in the liquid crystal community is increasingly focusing on highly inhomogeneous situations (behaviour near interfaces and solid surfaces, domain walls and defects, for example) so some consideration of atomic-scale effects is highly desirable.

Most liquid crystals of technological interest are formed by highly elongated molecules. In our simulation work we use a range of elementary molecular models. Typical examples are *ellipsoids of revolution* of length A, width B, elongation $e = A/B$; and *spherocylinders* of overall length $L + D$, width D. They are sufficient to describe the basic physics of liquid crystals; they all have a *nematic* phase, which will be the main object of study here. Given these basic shapes, the interaction potentials are divided into 'hard' and 'soft' classes: for *hard* potentials, the energy is infinite when two molecules overlap, and zero otherwise; for *soft* potentials, the energy varies continuously with relative position and orientation. We may improve these models by including attractive forces[6–10], biaxiality[11,12], nonlinearity[13], flexibility[14,15], dipolar forces[16] and hydrogen bonds[17]. Space permits us to touch on only one or two of these aspects in the present chapter.

Basic simulation methods are described in other chapters[18,19] and elsewhere[20,21], so only a brief summary of particular simulation strategies will be given in the following sections.

3 Theoretical Approaches

We shall be comparing some simulation results with theoretical predictions that may be expressed by writing down an approximate free energy *functional*. The functional may be assumed to depend on simple functions of particle positions and orientations, for instance the local single-particle density, the orientational order tensor, the direction of orientational ordering. All of these descriptions are coarse-grained: specification of the state of the system does not require knowledge of all of the N-particle microscopic coordinates. Instead, we must input the dependence of a handful of functions on the spatial and orientational coordinates, and minimize the free energy with respect to all possible variations of these functions.

The elastic theory due to Oseen and Frank[22,23] is based on writing part of the free energy $\mathcal{F}$ as a functional of the position-dependent liquid crystal director $\boldsymbol{n}(\boldsymbol{r})$:

$$\mathcal{F}_{\mathrm{OF}}\big[\boldsymbol{n}(\boldsymbol{r})\big] = \int_V \mathrm{d}^3\boldsymbol{r}\; f_b(\boldsymbol{r}) + \int_S \mathrm{d}^2\boldsymbol{s}\; f_s(\boldsymbol{s}) \tag{1a}$$

$$f_b(\boldsymbol{r}) = \tfrac{1}{2}K_{11}\big(\nabla\cdot\boldsymbol{n}\big)^2 + \tfrac{1}{2}K_{22}\big(\boldsymbol{n}\cdot\nabla\times\boldsymbol{n}\big)^2 + \tfrac{1}{2}K_{33}\big(\boldsymbol{n}\times\nabla\times\boldsymbol{n}\big)^2 \tag{1b}$$

$$f_s(\boldsymbol{s}) = \tfrac{1}{2}W_\theta \sin^2\theta \quad \text{where } \cos\theta = \boldsymbol{n}\cdot\boldsymbol{n}_s\ . \tag{1c}$$

where S is the surface bounding the sample volume V. There are two classes of terms: an integral, over V, of a bulk free energy density which depends on the splay (K_{11}), twist

(K_{22}) and bend (K_{33}) elastic constants; and an integral, over S, of a surface free energy density, which has been written here simply as a *surface anchoring* term of strength W_θ depending on the angle θ between $\boldsymbol{n}$ and the preferred anchoring orientation $\boldsymbol{n}_s$ at the surface. Omitted here are the surface-like elastic terms K_{13} and K_{24} which have been of recent experimental and theoretical interest[24–26].

The Frank free energy describes a nematic liquid crystal in regions where the *direction* of ordering is the only important variable, and where, moreover, it varies smoothly with position (hence it takes the form of a gradient expansion). A theory which allows the *degree* as well as the direction of ordering to vary is due to Landau and de Gennes[27], and is based on the 2nd-rank order tensor $\mathbf{Q}(\boldsymbol{r})$:

$$\mathcal{F}_{\mathrm{LdG}}[\mathbf{Q}(\boldsymbol{r})] = \int_V \mathrm{d}^3\boldsymbol{r}\ f_b(\boldsymbol{r}) + \int_S \mathrm{d}^2\boldsymbol{s}\ f_s(\boldsymbol{s}) \tag{2a}$$

$$f_b(\boldsymbol{r}) = \kappa\left|\nabla\mathbf{Q}\right|^2 + a\mathsf{Tr}\left[\mathbf{Q}^2\right] - b\mathsf{Tr}\left[\mathbf{Q}^3\right] + c\left\{\mathsf{Tr}\left[\mathbf{Q}^2\right]\right\}^2 \tag{2b}$$

$$f_s(\boldsymbol{s}) = w\mathsf{Tr}\left[\mathbf{Q}-\mathbf{Q}_s\right]^2 \tag{2c}$$

In the bulk free energy density, we see a one-constant representation of elastic behaviour (the squared gradient term), plus the leading terms in a free energy expansion, which would give a phenomenological description of the bulk I-N transition in the absence of gradients. To this may be added a surface anchoring term, the simplest form of which is exemplified by Eq. (2c), a square term involving the preferred order tensor $\mathbf{Q}_s$ at the surface.

The final theory to be considered here is that of Onsager[28] in which the free energy is written as a functional of the single-particle density $\varrho(\boldsymbol{r},\hat{\boldsymbol{a}})$:

$$\begin{aligned}\mathcal{F}_{\mathrm{Ons}}[\varrho(\boldsymbol{r},\hat{\boldsymbol{a}})] = {} & k_{\mathrm{B}}T\int \mathrm{d}^3\boldsymbol{r}\mathrm{d}^2\hat{\boldsymbol{a}}\ \varrho(\boldsymbol{r},\hat{\boldsymbol{a}})\left[\ln\varrho(\boldsymbol{r},\hat{\boldsymbol{a}})\Lambda^3 - 1 + u(\boldsymbol{r},\hat{\boldsymbol{a}})/k_{\mathrm{B}}T\right] \\ & - \tfrac{1}{2}k_{\mathrm{B}}T\iint \mathrm{d}^3\boldsymbol{r}_A\mathrm{d}^2\hat{\boldsymbol{a}}\ \mathrm{d}^3\boldsymbol{r}_B\mathrm{d}^2\hat{\boldsymbol{b}}\ \varrho(\boldsymbol{r}_A,\hat{\boldsymbol{a}})\varrho(\boldsymbol{r}_B,\hat{\boldsymbol{b}})\ f(\boldsymbol{r}_{AB},\hat{\boldsymbol{a}},\hat{\boldsymbol{b}})\ .\end{aligned} \tag{3}$$

Here, $\hat{\boldsymbol{a}}$, $\hat{\boldsymbol{b}}$ are the molecular orientation vectors; we assume uniaxial particles for convenience. The details of molecular shape and structure enter through the Mayer function $f(\boldsymbol{r}_{AB},\hat{\boldsymbol{a}},\hat{\boldsymbol{b}})$ which may be related directly to the intermolecular potential. Onsager's theory is a fore-runner of what we now call density functional theories. These have proved extremely successful in recent years when applied to simple atomic fluids[29–31], and have been used to explore liquid crystal phase diagrams[32]. In general, the functional $\mathcal{F}[\varrho]$ is unknown and nonlocal; the above expression is valid for low densities, but note that it is not restricted to smooth variations of $\varrho(\boldsymbol{r},\hat{\boldsymbol{a}})$. An empirical improvement of Onsager's theory, due to Parsons and Lee[33–35], introduces a density-dependent prefactor into the two-body term, and extends its range of validity to higher densities.

4 Liquid Crystal Phase Diagrams

4.1 Hard-Particle Systems

It is twenty years since the phase diagram of the hard ellipsoid system was determined by Frenkel and Mulder[36] and the role of their follow-up paper[37] in shaping the future development of the field is concisely summarised by Evans[38]. Their results are shown

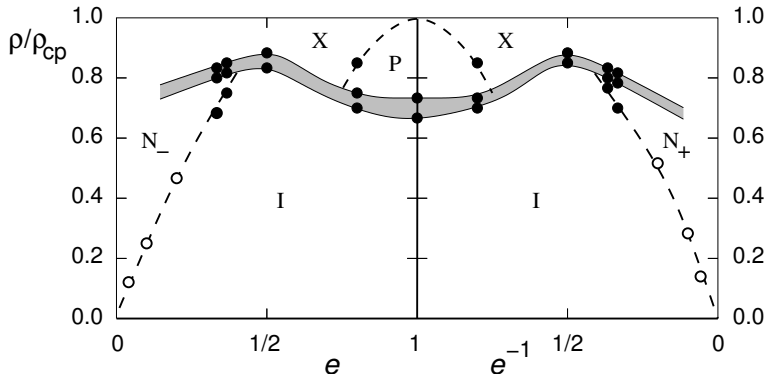

Figure 1. Schematic hard ellipsoid phase diagram as a function of elongation e (on a reciprocal scale for $e > 1$), and density ρ (as a fraction of the close-packed density ρ_{cp}). The isotropic (I), crystalline (X), plastic crystalline (P), nematic (N_+) and discotic (N_-) phases are indicated. The solid-fluid coexistence region is shaded, and the I-N and P-X transitions indicated by dashed lines. The state points studied in Refs. 36, 37 are indicated by filled circles.

schematically in Fig. 1. This work involved determination of free energies and chemical potentials by thermodynamic integration with respect to an external orienting field. Recall, to locate a phase transition, it is necessary to determine the state points which satisfy that conditions for thermodynamic equilibrium: $T_1 = T_2$, $P_1 = P_2$, $\mu_1 = \mu_2$. For particles interacting only with infinitely repulsive potentials, the temperature is not a significant thermodynamic variable, and the first equality is always satisfied. The last equation is the most difficult to determine.

Subsequent studies of ellipsoids at higher elongations[39] involved a range of techniques: (a) test particle insertion plus thermodynamic integration; (b) simulation in the Gibbs ensemble; (c) thermodynamic integration with respect to changes in particle shape; (d) tracing phase coexistence boundaries using Clapeyron-like equations; and it is instructive to consider these in more detail.

The chemical potential at a point (T, P) in each phase may be found by Widom test particle insertion. Since $\mu^{\text{ex}} = F^{\text{ex}}_{N+1} - F^{\text{ex}}_{N}$,

$$\beta\mu^{\text{ex}} = -\ln\langle\exp(-\beta\mathcal{U}_{\text{test}})\rangle$$

where $\mathcal{U}_{\text{test}}$ is the potential energy of interaction of a randomly inserted test particle with the N particles in the system (in this case, $\mathcal{U}_{\text{test}}$ is either infinity or zero, so the exponential is either zero or one). Then one may use thermodynamic integration

$$\mu(P) = \mu(P_0) + \int_{P_0}^{P} \rho^{-1}\,\mathrm{d}P$$

to solve $\mu_1(P_1) = \mu_2(P_2)$.

Automatic equilibration of two phases, with each phase in its own simulation box, may be achieved using the Gibbs ensemble method of Panagiotopoulos[40,41]. Briefly, this technique involves standard Monte Carlo moves in each box; volume exchange moves between boxes, which guarantee $P_1 = P_2$; and particle transfer moves arranged to ensure

$\mu_1 = \mu_2$. Both the Widom method and the Gibbs ensemble method work well at low-to-moderate densities, and this is the case for the I-N transition for highly elongated, $e = 20$, hard ellipsoids, as demonstrated in Fig. 2.

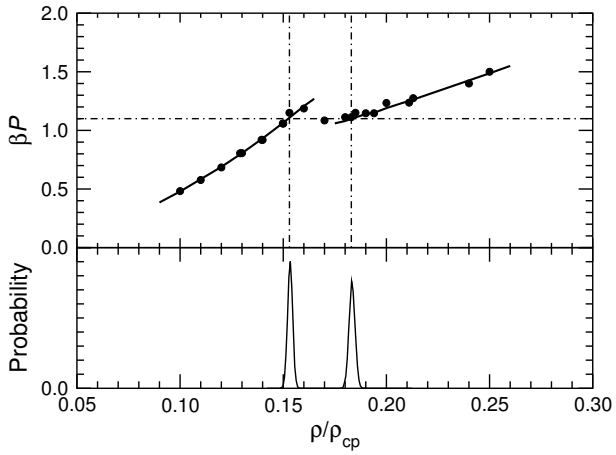

Figure 2. I-N coexistence for $e = 20$ ellipsoids. The data points with solid lines are the equations of state $P(\rho)$ for isotropic and nematic phases, with the coexistence value $P_{\rm NI}$ determined by Widom test-particle insertion plus thermodynamic integration, indicated by dot-dashed lines. Below this is the probability distribution function for density ρ averaged over both boxes in a Gibbs simulation.

For dense fluids, both the Widom method and the Gibbs ensemble become less reliable, due to the low acceptance rates for particle insertion. One solution is to use an *expanded ensemble* in which N-particle and $(N + 1)$-particle systems are linked by intermediate fractional-particle states[42,43]. One particle is scaled in size by a parameter κ, taking values $0 \leq \kappa \leq 1$. In the Monte Carlo procedure, we allow transitions between species $\kappa \rightleftharpoons \kappa'$. We determine the probability histogram $\mathcal{P}(\kappa)$, and hence the relative free energies of species $\mathcal{F}(\kappa)$; then $\mathcal{F}(1) - \mathcal{F}(0)$ gives $\mu^{\rm ex}$. To ensure uniform sampling of species, we apply an (iteratively refined) weighting function $\mathcal{W}(\kappa)$ to the κ-moves. It is essential that the scaled particle samples fluid configurations efficiently. To assist, we introduce two additional types of move which dramatically relocate it. Firstly, we attempt to move the scaled particle to a completely random position, as in the (random-insertion) Widom method. Such moves are accepted with high probability when κ is small. Secondly, we attempt to exchange the scaled particle with full-size particles. This works best when κ is large. Details are given elsewhere[39].

An essential part of a study of this kind is to determine how the transition pressure changes as we slowly vary molecular shape, or some other parameter. The idea is to avoid computing chemical potentials from scratch, for each case. A useful approach, due to Kofke[44], is to derive and then use a variant of the Clapeyron equation. Suppose we characterize the molecular shape by a parameter λ; here we choose $\lambda = \ln a$ ($a =$ length) or $\ln b$ ($b =$ width) for convenience. Then we define a thermodynamic variable $\Gamma = (\partial\mu/\partial\lambda)_{TP}$ conjugate to λ; this means that we may write $\mathrm{d}\mu = \Gamma \mathrm{d}\lambda + v\mathrm{d}P$. It follows

that

$$\frac{\mathrm{d}P}{\mathrm{d}\lambda} = -\frac{\Delta\Gamma}{\Delta v} \quad \text{or} \quad \frac{\mathrm{d}\ln P}{\mathrm{d}\lambda} = -\frac{\Delta\Gamma}{P\Delta v} \, .$$

Kofke's method consists of evaluating the terms on the right, and integrating step-by-step with respect to λ along the coexistence curve. Applying these techniques to the hard ellipsoid system[39], we were able to show the extent of applicability of both Onsager and Parsons theories, and the expected decrease in strength of transition on decreasing elongation, as shown in Fig. 3. The effects of molecular biaxiality on the phase diagram have recently been investigated in the same way using a hard spheroid model[12].

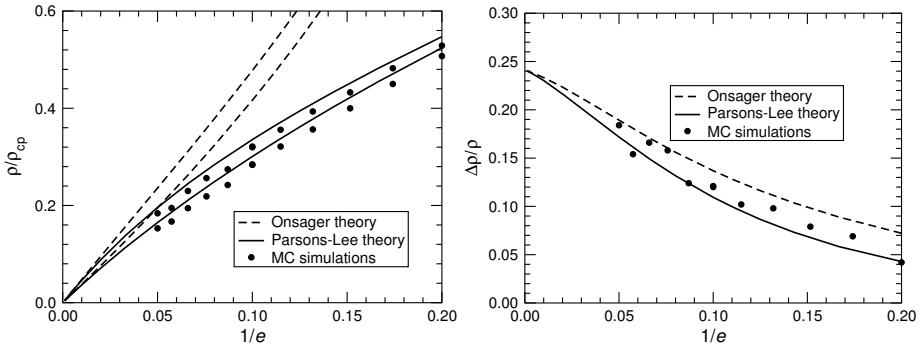

Figure 3. Coexistence densities (left) and fractional density change (right) at the I-N transition vs elongation for hard ellipsoids of revolution. For details see Ref. 39.

4.2 Rod-Plate Mixtures

Mixtures of rod-like and plate-like molecules may form isotropic, uniaxial and biaxial phases as shown in Fig. 4. The biaxial phase competes with demixing into two uniaxial phases: this is an example of phase separation due to soley repulsive interactions. We have studied mixtures of ellipsoids of the same molecular volume, and two conjugate pairs of shapes: $e = 15, 1/15$ and $e = 20, 1/20$ to investigate this competition. Once again it was possible to compare with Onsager theory and the Parsons-Lee rescaling. The phase transitions were located by performing Gibbs ensemble simulations, and observing the behaviour of order parameters characterizing both phases; full details are given elsewhere[45]. The phase diagram for the $e = 15, 1/15$ system is shown in Fig. 5 (that for $e = 20, 1/20$ is similar). A striking feature is the asymmetric line separating the biaxial phase from the two-phase demixing region. For these conjugate shapes, a symmetry of the second virial coefficient under the exchange $e \leftrightarrow 1/e$ means that the phase diagram predicted by the Onsager or Parsons theory is symmetric about the 50:50 composition. Most of the phase boundaries exhibit this symmetry, approximately, but the dividing line between biaxial and two-phase regions is clearly very sensitive to three-body, or perhaps higher, interactions.

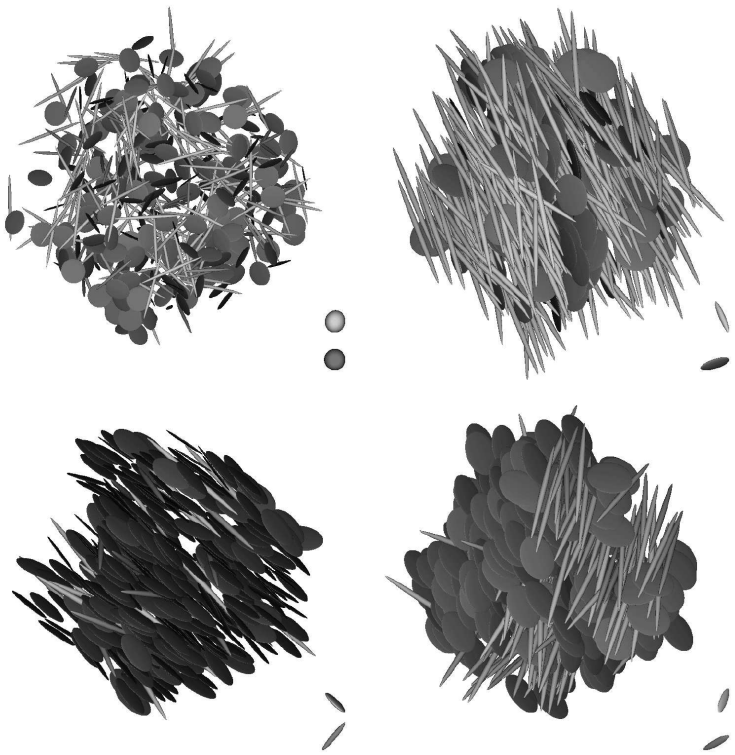

Figure 4. Rod and plate configurations for $e = 20, 1/20$ ellipsoid mixtures, showing isotropic, uniaxial nematic, discotic and biaxial phases. The biaxial configuration also shows some demixing. At the bottom right corner of each configuration, two spheroids give a visual representation of the orientational ordering of rods (upper) and plates (lower).

4.3 The Gay-Berne Model

The introduction of attractive forces into the molecular model makes the phase diagram a little more realistic, but more complicated. The well-known Gay-Berne potential has become a standard model for the study of liquid crystalline phases. The molecular pair potential

$$v_{AB} = 4\varepsilon(A,B)\left[\left(\frac{\sigma_0}{r_{AB}-\sigma(A,B)+\sigma_0}\right)^{12} - \left(\frac{\sigma_0}{r_{AB}-\sigma(A,B)+\sigma_0}\right)^{6}\right]$$

depends upon the molecular axis vectors $\hat{\boldsymbol{a}}$ and $\hat{\boldsymbol{b}}$, and on the direction $\hat{\boldsymbol{r}}_{AB}$ and magnitude r of the centre-centre vector $\boldsymbol{r}_{AB} = \boldsymbol{r}_A - \boldsymbol{r}_B$. The parameter σ_0 determines the smallest molecular diameter and there are two orientation-dependent quantities: a diameter $\sigma(A,B) = \sigma\big(\hat{\boldsymbol{r}}_{AB}, \hat{\boldsymbol{a}}, \hat{\boldsymbol{b}} \mid \kappa, \kappa', \mu, \nu\big)$ and an energy $\varepsilon(A,B) = \varepsilon\big(\hat{\boldsymbol{r}}_{AB}, \hat{\boldsymbol{a}}, \hat{\boldsymbol{b}} \mid \kappa, \kappa', \mu, \nu\big)$. Each quantity depends in a complicated way (not given here) on the shape anisotropy parameter κ, the energy anisotropy parameter κ', and two exponents μ, ν. The original 'reference' model has $\mu = 2$, $\nu = 1$, $\kappa = 3$, $\kappa' = 5$.

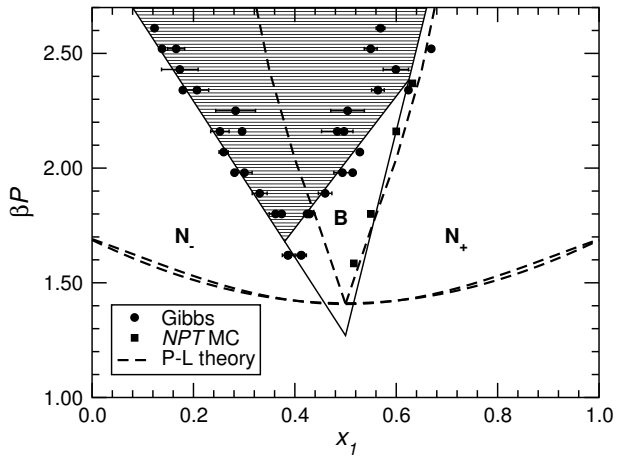

Figure 5. Phase diagram for $e = 15, 1/15$ rod-plate mixtures in the pressure-composition plane: x_1 is the mole fraction of rods. The points are simulation results, the solid lines mark approximate phase boundaries, the two-phase region is shaded, and the dashed-lines are the predictions of Parsons-Lee theory. For further details see Ref. 45.

The effects of varying the attractive anisotropy parameter κ' in the range $1 \leq \kappa' \leq 25$, with fixed $\kappa = 3$, have been reported in detail[46,9]. Perhaps the most interesting effect is the growth of the liquid-vapour coexistence envelope on reducing κ', as illustrated in Fig. 6. The envelope was determined by Gibbs ensemble simulation, but this became

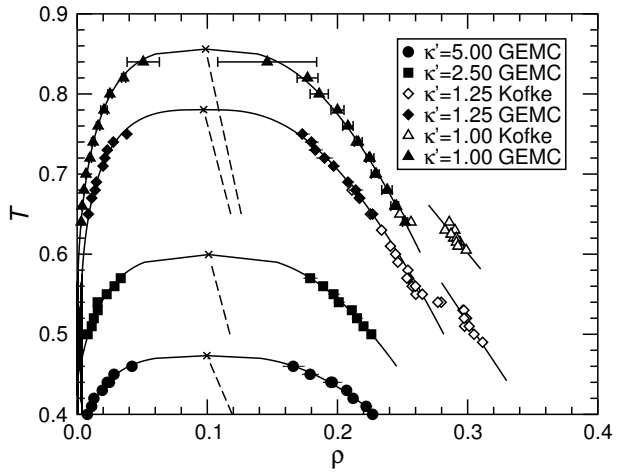

Figure 6. The effects of varying the anisotropy of the attractive forces in the Gay-Berne potential on the liquid-vapour coexistence envelope. Shown are the results of Gibbs simulations and Kofke (Gibbs-Duhem) integration. There is an I-N transition on the liquid branch for $\kappa' = 1.00$ and 1.25.

less efficient at lower temperatures as the liquid density became higher; just at this point,

evidence emerged of an I-N transition on the liquid side, raising the prospect of being able to simulate a nematic-vapour interface. The coexisting vapour density is very low at these temperatures, so a constant-pressure simulation with $P = 0$ provides a good guide to the behaviour of the liquid with changing temperature; however, it was also possible to conduct thermodynamic integration using the Kofke method, to determine both vapour and liquid densities at coexistence. Studies of the nematic-vapour interface for this model have been undertaken by two groups[46–48].

Values of the elongation κ in the range $3 \leq \kappa \leq 4$ with fixed $\kappa' = 5$ have also been studied[10]. The effects of increasing κ from 3 to 4 are indicated in the phase diagrams of Fig. 7. The liquid-vapour envelope contracts and disappears, while the layered smectic-A phase becomes stable, but bounded at high and low T. Further details, including a discussion of methods for identifying the various smectic phases and distinguishing them from the crystalline state, may be found in Ref. 10.

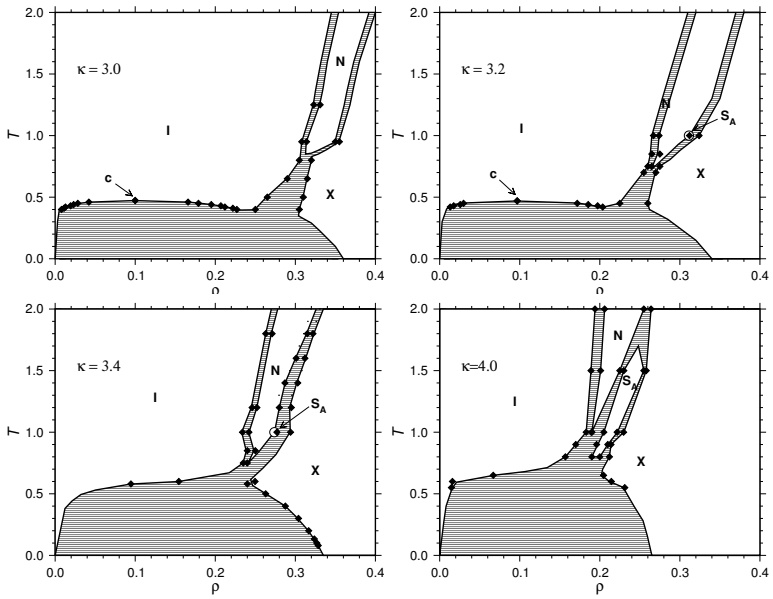

Figure 7. Schematic phase diagrams for Gay-Berne systems at various elongations. For more details see Ref. 10.

5 Dynamics of Liquid Crystals

An early and surprising result of molecular dynamics simulation of hard ellipsoids, was that for some elongations, in the vicinity of the isotropic-nematic transition, the component of the single-particle diffusion coefficient parallel to the director would *increase* with increasing density[49]. Subsequently, it proved possible to correlate this with the rapidly changing order parameter near the transition point[50]: roughly speaking, as the system becomes more ordered, diffusion of a molecule along its length becomes less and less hindered by collisions with its neighbours.

Collective dynamics, and the growth of large, highly-ordered regions on the approach to the isotropic-nematic transition temperature $T_{\rm NI}$ are also of interest. From the isotropic side, the correlation length for second-rank orientational fluctuations ξ_2 diverges and collective orientational dynamics become slow, rather like density fluctuations near the liquid-vapour critical point. The extrapolated divergence temperature T^* is very slightly lower than the thermodynamic transition temperature, and the transition is weakly first-order rather than being continuous. Although a proper system-size dependent study of this phase transition would be very expensive, and is only really feasible for a lattice model[51,52], there is some interest in observing pre-transitional fluctuations using a molecular model and comparing with simple theoretical predictions. We studied a system of $N = 8000$ molecules, interacting with a version of the Gay-Berne potential[8], using typical run lengths ~ 20 ns. For temperatures just above the transition temperature we have studied structural correlations and dynamical correlation functions[53]. The static pair correlation function, $h(1,2)$, and the direct correlation function, $c(1,2)$, may be expanded in a set of rotationally invariant functions[54] to obtain some insight into the slowing down. Our results, shown in Fig. 8 suggest that, as expected, the appropriate components of $c(1,2)$ remain short-ranged (at least, for the temperatures investigated here) while the corresponding components of $h(1,2)$ develop long-ranged correlations.

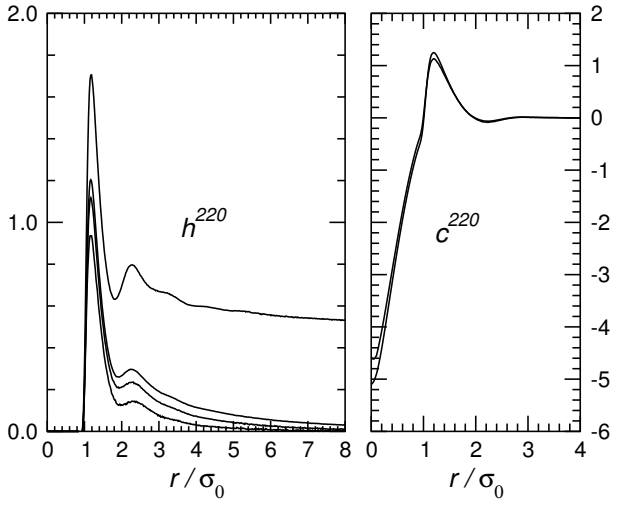

Figure 8. On the left we show the component of the total correlation function $h^{220}(r)$ which shows pretransitional growth of orientational correlations, approaching the I-N transition at $T = 4.0, 3.6, 3.5$ and at $T = 3.45$, below the transition, showing long-ranged order. On the right we show the corresponding component of the direct correlation function, $c^{220}(r)$, approaching the transition at $T = 4.0, 3.5$.

To study the collective dynamics we defined a variable

$$Q_{\alpha\beta}(\boldsymbol{k},t) = \sum_i \left(\frac{3}{2} u_{i\alpha}(t) u_{i\beta}(t) - \frac{1}{2}\delta_{\alpha\beta} \right) \mathrm{e}^{\mathrm{i}\boldsymbol{k}\cdot\boldsymbol{r}_i(t)} \qquad \alpha,\beta = x,y,z \qquad (4)$$

and measured the time correlation function

$$C(k,t) = \sum_{\alpha\beta} \langle Q_{\alpha\beta}(-\boldsymbol{k},0) Q_{\alpha\beta}(\boldsymbol{k},t)\rangle \propto \sum_{ij} \left\langle P_2(\hat{\boldsymbol{a}}_i(0)\cdot\hat{\boldsymbol{a}}_j(t))\, \mathrm{e}^{\mathrm{i}\boldsymbol{k}\cdot(\boldsymbol{r}_i(0)-\boldsymbol{r}_j(t))}\right\rangle$$

From the simulation results we observed roughly exponential decay

$$C(k,t) = A(k)\exp\{-t/\tau(k)\}$$

with $\tau(k) \sim k^{-2}$. At $k = 0$, we found $\tau^{-1} \propto \xi_2^{-2} \propto (T - T^*)$, in agreement with a simple Landau-de Gennes description[27]. For further details see Ref. 53.

6 Elastic Properties

The simulation of truly large-scale phenomena associated with elastic deformations of the director field requires parallel computing resources, and the programs used for the work described in the following sections were developed as a consortium project within the U.K. High Performance Computing Initiative. The parallel MD code developed in this project is described elsewhere[55].

6.1 Bulk Elastic Constants

Long-wavelength deformations of the director field $\boldsymbol{n}(\boldsymbol{r})$ are described by the Frank free energy (1). The question to be addressed here is 'Can simulation provide values of the coefficients in this expression?'.

In the nematic phase, for sufficiently long wavelengths that the elastic picture holds, equilibrium thermal fluctuations of the Fourier-transformed orientation density $\hat{Q}_{\alpha\beta}(\boldsymbol{k})$ (defined by Eq. (4)) are determined by the elastic constants. It is convenient to define the following:

$$\mathcal{W}_{13}(k_1,k_3) \propto \left\langle \hat{Q}_{13}(\boldsymbol{k})\hat{Q}_{13}(-\boldsymbol{k})\right\rangle^{-1} \equiv \langle|\hat{Q}_{13}(\boldsymbol{k})|^2\rangle^{-1} \propto K_1 k_1^2 + K_3 k_3^2$$

$$\mathcal{W}_{23}(k_1,k_3) \propto \left\langle \hat{Q}_{23}(\boldsymbol{k})\hat{Q}_{23}(-\boldsymbol{k})\right\rangle^{-1} \equiv \langle|\hat{Q}_{23}(\boldsymbol{k})|^2\rangle^{-1} \propto K_2 k_1^2 + K_3 k_3^2$$

Here, the director is chosen to lie in the 3-direction; $\boldsymbol{k} = (k_1, 0, k_3)$ is in the 1-3 plane. These quantities may be determined in a standard computer simulation, and a fit made to $\mathcal{W}_{13}$ and $\mathcal{W}_{23}$ as functions of k_1^2 and k_3^2. Taking the low-k limit is the crucial part of this process, so it is essential to have a large enough simulation box size L to guarantee the accuracy of the extrapolation. It is convenient to constrain the 123 axis system to coincide with the xyz coordinate system of the simulation box, otherwise the components k_1, k_3 will change as the director drifts; this can be done using Lagrangian constraints in molecular dynamics. We have studied[56] the Gay-Berne potential[57,8]. Slow fluctuations of the long-wavelength modes necessitated long simulation runs, while system sizes up to $N = 8000$ particles were used to guarantee the correctness of the low-k extrapolation. Typical slices through the fitted surface, with the corresponding data points, are shown in Fig. 9.

The key conclusions of this work were that elastic constants can indeed be measured quite accurately by this method, and that the absolute magnitudes of the elastic constants,

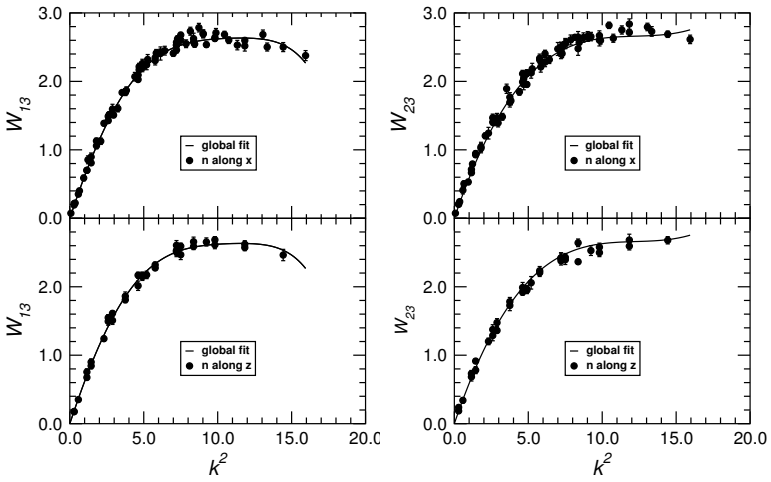

Figure 9. Splay (left) and twist (right) fluctuations as functions of wavelength for the Gay-Berne model with $\mu = 2, \nu = 1, \kappa = 3, \kappa' = 5$ at $\rho = 0.32, T = 0.90$. Here the wave-vector component along the director k_3 is taken to be zero, and the inverse fluctuations quantities $\mathcal{W}_{13}$ and $\mathcal{W}_{23}$ are plotted as functions of k_1^2. The solid lines show sections through the globally-fitted surface. For more details see Ref. 56.

and their ratios, are consistent with those expected for rod-like molecules. In particular the bend elastic constant K_{33} was typically rather larger than the other two, and the values were all reasonably close to those found for hard ellipsoids of similar shape, at comparable densities.

6.2 Surface Anchoring Strengths

Simulation and theory have been used[58,59] to explore the anchoring of a liquid crystal at a solid surface. To begin with, we consider a simple 'experimental' geometry, in which the liquid crystal is confined between two walls: at one wall an orienting field is applied, and the response of the director alignment across the cell is measured, with the aim of calculating the strength of anchoring at the opposite wall. In keeping with the simple molecular model, namely hard ellipsoids of elongation $A/B = 15$, the wall-molecule interaction is a very idealized hard potential, defined simply by the condition that the centres of the molecules may not pass through it. Purely entropic considerations, having their origin in the way molecules pack together, generate homeotropic (normal) anchoring. Experimentally, it is quite common to anchor liquid crystals at a treated interface, in which a layer of organic molecules is adsorbed on the solid surface. The liquid crystal molecules partially penetrate the organic layer: the effect of this is modelled (albeit in a simple way) by the chosen boundary condition.

The wall anchoring coefficient W measures the strength with which the surface resists director deformation away from the preferred direction. The approach used in the simulation to measure this is illustrated in Fig. 10. The key quantity turns out to be the *extrapolation length* $\lambda = K_{33}/W$, measurable by fitting director profiles to the elastic theory. For $A/B = 15$ ellipsoids, λ is of the order of one molecular length, as shown in Fig. 11.

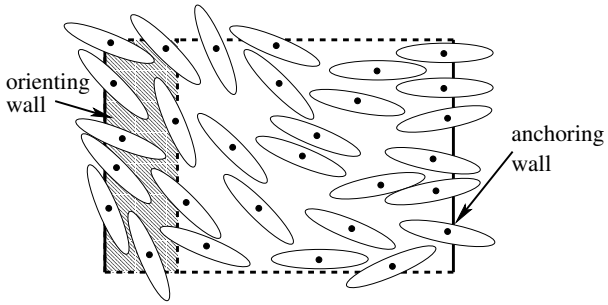

Figure 10. Schematic picture of simulation to measure wall anchoring coefficient W. At the left wall, a strong, but short-ranged, orienting field is applied in the shaded region to fix the nematic director in a chosen direction. The director profile is measured across the cell: in the elastic theory, it is determined by the surface anchoring coefficient at the right wall, W, and the bulk splay and bend elastic constants K_{11}, K_{33}

Direct minimization of the Onsager free energy functional, with essentially no adjustable parameters, reproduces these director profiles very well, *even in the wall regions where the elastic theory is inaccurate.* In the above treatment, it was assumed that the positions of

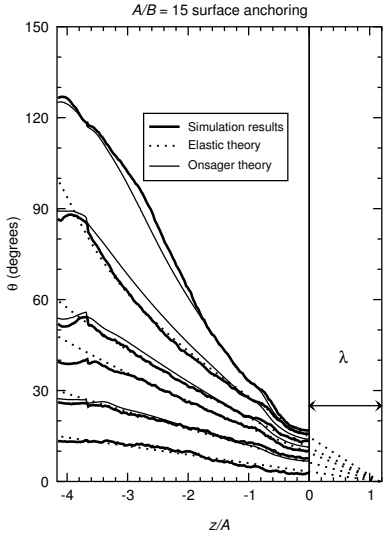

Figure 11. Simulation results, elastic theory fits, and predictions of Onsager theory to determine the extrapolation length λ, and hence the surface anchoring coefficient W. Several different anchoring angles are imposed at the left wall. The curvature in the profiles is because the deformation is predominantly splay as $\theta \rightarrow 90^\circ$ and predominantly bend as $\theta \rightarrow 0^\circ$: the two elastic constants are different (After Ref. 58).

the elastic-theory boundary conditions coincide with the hard potential walls. There is no reason, in principle, why this should be so, although we would expect the difference in positions to be a molecular length rather than a mesoscopic length. This difference turns

out to be detectable when one studies fluctuations of the director $\boldsymbol{n}(\boldsymbol{r})$ in slabs of varying thickness between identical walls[60].

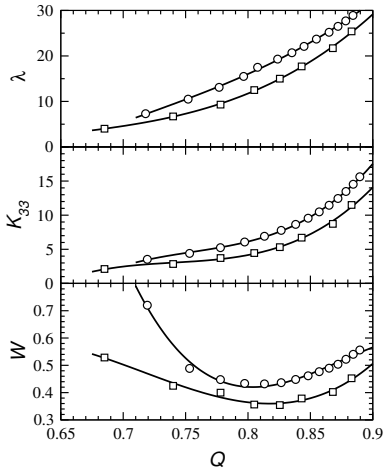

Figure 12. Extrapolation length λ, bend elastic constant K_{33} and anchoring strength W, as functions of order parameter Q. We show the results of Onsager theory (circles) and Monte Carlo simulations (squares) (After Ref. 61).

For this model, the anchoring coefficient varies in an interesting way with density or, equivalently, nematic order parameter. From the available experimental data on thermotropic liquid crystals, one can say that the extrapolation length $\lambda = K_{33}/W$ is inversely proportional to the squared value of the bulk order parameter $\lambda \propto Q^{-2}$. Taking into account that the elastic constant K_{33} is typically proportional to Q^2, this gives[62] for the anchoring parameter $W \propto Q^4$. However, our simulations and Onsager theory do not conform to this model. The dependences of λ, K_{33}, and W on the order parameter Q are shown in Fig 12. Rather than decreasing, the extrapolation length λ *increases* with Q, albeit not as strongly as K_{33}. The net result is that $W = K_{33}/\lambda$ has a non-monotonic dependence on Q, first decreasing, then increasing, although the variation is not dramatic. It turns out that this behaviour is connected with the variation of the density profile in the immediate vicinity of the surface, which is often neglected in theoretical treatments. Further details may be found in Ref. 61.

7 Nematic-Isotropic Interface

Now we consider what happens when the nematic and isotropic phases are at coexistence, either with or without the confining effect of walls. The N-I interface is one of the simplest fluid-fluid interfaces and poses some interesting basic questions. The simulation of this interface requires great care: the coexisting densities are typically very similar, and the surface tension will be relatively small, so fluctuations may be important. Our interest here lies in the determination of the properties of the nematic-isotropic interface, including the

surface tension, while taking care to allow all the fluctuations associated with thermal equilibrium. We have studied[63] a thick film of nematic phase adsorbed on a solid wall with the same kind of boundary conditions discussed earlier; the system is illustrated schematically in Fig. 13.

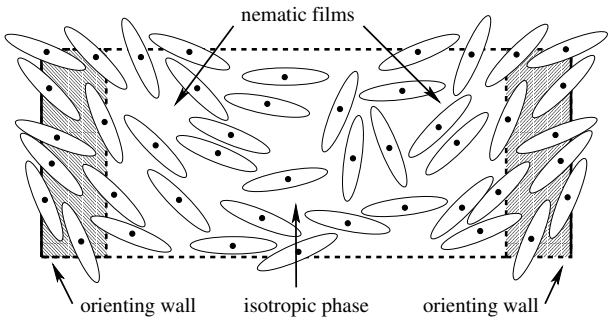

Figure 13. Schematic picture of simulation to investigate the isotropic-nematic interface, with director orientation controlled by anchoring at the confining walls. At the hard walls, strong, but short-ranged, orienting fields are applied to fix the nematic director in a chosen direction. The two wall anchoring conditions may be chosen independently, provided the isotropic region in the middle is sufficiently wide

7.1 Orientational Order and Density Profiles

For an isolated surface, the film thickness is determined by the deviation of the chemical potential from the bulk coexistence value $\mu - \mu_{\rm IN}$. In a closed, confined system with adsorbed films on both walls, assuming the wall separation is large enough that the two films are essentially independent, the film thickness is determined by the overall density. The phase transitions in this type of system, such as the wetting behaviour, and the nematic-isotropic equivalent of 'capillary condensation', are of great interest[64,65]; but here the focus of attention will be the structure of the nematic film and the interface between the two fluid phases.

We have, once more, studied ellipsoids of molecular elongation $A/B = 15$. Figure 14 gives an example of the order parameter and density profiles obtained by simulation, and compared with Onsager theory predictions, for the case when the orienting field at the hard wall aligns the director in the plane of the wall, i.e. at 90° to the interface normal. The agreement between theory and simulation is good, bearing in mind that Onsager theory is known to overestimate the bulk coexistence densities; indeed, very detailed comparisons of the profile shapes may be made[63].

There is some interest in studying even longer molecules[66]. Firstly, it has been predicted using Onsager theory for infinitely long rods[67] that the number density $\rho(z)$ varies in a significantly non-monotonic way near the I-N interface, for the lowest free energy case of in-plane alignment. There is no evidence of this for $A/B = 15$, in either simulation or theory (see Fig. 14), which raises the possibility that the effect is only seen for higher elongations. Secondly, again for this alignment, the orientational ordering near the interface should be *biaxial*: symmetry is broken in two directions, namely normal to the

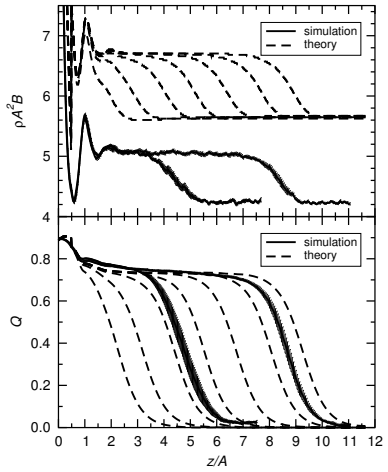

Figure 14. Profiles of number density in reduced units $\rho A^2 B = N A^2 B/V$, and order parameter Q (largest eigenvalue of the order tensor $\mathbf{Q}$), for a nematic film anchored at 90° to the normal at the left wall (in-plane alignment), in equilibrium with the isotropic phase. Simulation results are given for two different film thicknesses (solid line with error bars) and Onsager theory predictions for seven different film thicknesses (dashed lines) (After Ref. 63).

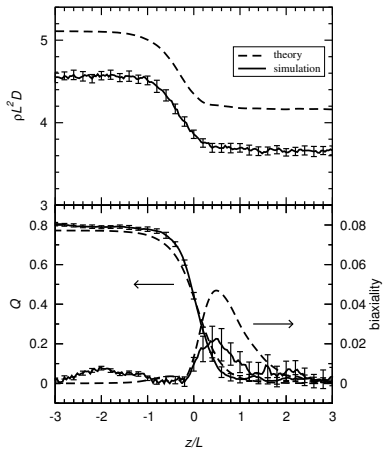

Figure 15. Profiles of reduced number density $\rho L^2 D$, orientational order parameter Q, and orientational biaxiality (on a $\times 10$ expanded scale), in the vicinity of the I-N interface, for $L/D = 50$ soft spherocylinders, determined by simulation (solid lines with error bars) and from Onsager theory (dashed lines) (After Ref. 66).

interface, and in the plane of the interface along the director. However, this biaxiality is extremely small for the $A/B = 15$ elongation described earlier. In Fig. 15 are the relevant profiles for a soft spherocylinder model with length/width = $L/D = 50$, studied by molecular dynamics, using a free-standing nematic film surrounded by isotropic phase in fully periodic boundaries. It can be seen that the density profile changes monotonically,

both in simulation and theory. However, the biaxiality (defined as the difference between the middle and lowest eigenvalues of the order tensor $\mathbf{Q}$) is detectable in the simulation, and is overestimated by the Onsager theory by about a factor of 2.

7.2 Surface Tension

One of the most important characteristics of an interface is the surface tension or surface free energy γ. For the I-N interface, the variation of this quantity with director angle gives, essentially, the anchoring potential at the interface. It will dictate the shape of droplets of one phase suspended in the other. Determining this quantity for an equilibrium I-N interface is a significant challenge for computer simulation. For a planar interface normal to the z-direction, a microscopic expression for surface tension γ is:

$$\gamma = \int_{-\infty}^{\infty} \mathrm{d}z \, \left[P_{\parallel} - P_{\perp}(z) \right] \equiv \int_{-\infty}^{\infty} \mathrm{d}z \, \pi(z) \, .$$

Here, $P_{\parallel} = P_{zz} = P$ is the normal component of the pressure tensor, which is independent of z throughout the system; $P_{\perp}(z) = P_{xx}(z) = P_{yy}(z)$ is the transverse component of the pressure tensor, and this varies with z near interfaces. Far from the interface, $P_{\perp}(z) = P_{\parallel} = P$. In the above formulae, the microscopic definition of $P_{\perp}(z)$ is not unique, although the value of the surface tension does not depend on the choice[68–70] and in the following it turns out that the differences in the profiles are quite small[71].

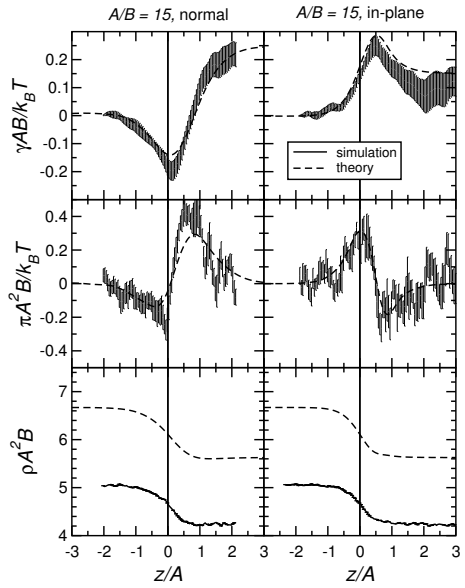

Figure 16. Profiles of number density ρ, pressure tensor difference $\pi(z)$, and running integral $\int \pi(z)\,\mathrm{d}z$ (which gives the surface tension γ), all in appropriate reduced units. Director alignment is normal to the interface or in the plane of the interface, as indicated. $A/B = 15$ hard ellipsoids. Simulation results are represented by error bars, calculated from 8 independent simulations, and the predictions of Onsager theory are represented by dashed lines (After Ref 72).

The pressure tensor profiles for the I-N interface of hard and soft ellipsoids with $A/B = 15$ are measurable in simulation, taking care to eliminate systematic errors, finite size effects, and statistical fluctuations[72]. The results are shown in Fig. 16. Several interesting things emerge. The simulation results are quite noisy, but they are confirmed in detail by the Onsager theory; the surface tension of the in-plane orientation is indeed found to be lower than for normal alignment; and most dramatically, the curves for the two director orientations are qualitatively different in character. For in-plane alignment, the tension appears on the nematic side of the interface, and there is a small compressive region on the isotropic side, reducing the eventual value of γ somewhat. The net effect is that the surface of tension, defined by the first moment of the pressure tensor profile, is about one molecule length away from the interface on the nematic side. For normal alignment, the tension appears on the *isotropic* side, and there is some compression on the nematic side; the surface of tension is a significant distance, about two molecule lengths, from the interface on the isotropic side.

7.3 Capillary Waves

The Onsager theory *neglects* capillary wave fluctuations of the interface; these are also suppressed in computer simulations with insufficient transverse box dimensions. However, they may be detected in much larger-scale simulations[73]. Suppose that we split the simulation box, of overall dimensions $L_\perp \times L_\perp \times L_z$ into blocks (columns) of transverse dimension $\ell_\perp \times \ell_\perp$ and length L_z; for each block we measure the deviation $h(x, y)$ of the interfacial position from its average. The capillary wave Hamiltonian is given by the quadratic form:

$$\mathcal{H}_{\text{CW}} = \frac{\gamma}{2} \int \int \mathrm{d}x \mathrm{d}y \left[\left(\frac{\partial h}{\partial x} \right)^2 + \left(\frac{\partial h}{\partial y} \right)^2 \right] = \frac{\gamma}{2} \sum_{\boldsymbol{q}_\perp} q_\perp^2 |h(\boldsymbol{q}_\perp)|^2$$

with transverse wave-vector $\boldsymbol{q}_\perp = (q_x, q_y)$. Hence $\left\langle |h(\boldsymbol{q}_\perp)|^2 \right\rangle = k_{\text{B}}T/\gamma q_\perp^2$ and the local mean-squared deviation of the interface may be obtained:

$$s^2 = \langle h^2(x, y) \rangle = \frac{1}{4\pi^2} \int \mathrm{d}\boldsymbol{q}_\perp \, \langle |h(\boldsymbol{q}_\perp)|^2 \rangle = \frac{k_{\text{B}}T}{2\pi\gamma} \ln \left(\frac{q_{\text{max}}}{q_{\text{min}}} \right)$$

with $q_{\text{min}} = 2\pi/L_\perp$, $q_{\text{max}} = 2\pi/\ell_\perp$. We expect a Gaussian distribution

$$P(h) = (2\pi s^2)^{-1/2} \exp(-h^2/2s^2) \, .$$

Moreover the intrinsic thickness of the interface, t_0, will be broadened, within a block of transverse dimension $\ell_\perp$, by capillary waves as follows

$$t^2 = t_0^2 + \frac{\pi}{2} \hat{s}^2 = t_0^2 + \frac{k_{\text{B}}T}{4\gamma} \ln \left(\frac{\hat{q}_{\text{max}}}{\hat{q}_{\text{min}}} \right)$$

where $\hat{q}_{\text{min}} = 2\pi/\ell_\perp$ and $\hat{q}_{\text{max}} \sim 2\pi/a_0$, $a_0 =$ a microscopic length.

We studied a system of $N = 115200$ soft ellipsoids with $A/B = 15$, in a periodic box with dimensions $L_x = L_y = L_\perp \approx 150B$ and $L_z \approx 300B$. A nematic-isotropic film system was prepared and allowed to stabilize with the director assuming the preferred planar orientation: 1.2×10^6 MD steps were allowed for equilibration, and $\sim 2.0 \times 10^6$ MD

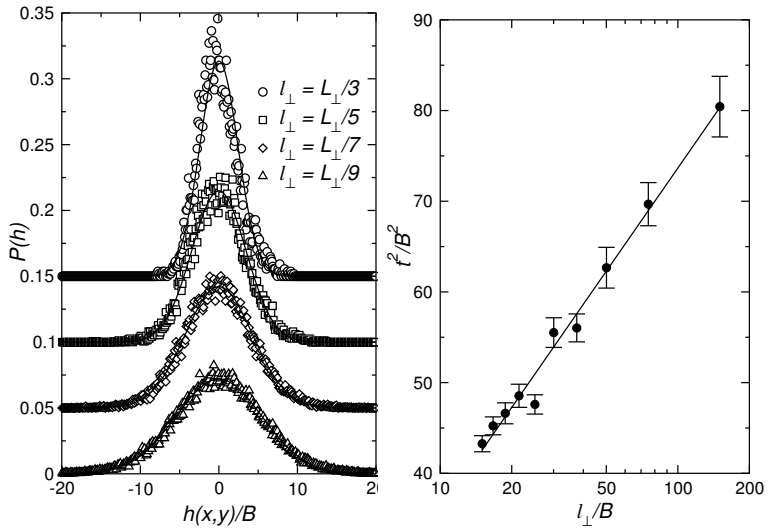

Figure 17. **Left:** Probability distribution for interface height $P(h)$ averaged over blocks of various transverse dimensions (indicated). Curves are displaced vertically for clarity. **Right:** Mean squared interfacial thickness t^2 as a function of transverse dimensions of blocks (log scale) (After Ref. 73).

steps to collect data. The local interfacial position distribution $P(h)$ is shown in Fig. 17: it is fitted well by the Gaussian distribution. The squared interfacial thickness, t^2, is plotted as a function of block size $\ell_\perp$, in Fig. 17. Particularly at large $\ell_\perp$, the dependence of t^2 on $\ell_\perp$ is logarithmic, which is consistent with the capillary wave picture. The interfacial tension estimated from this logarithmic dependence is in reasonable agreement with the values obtained from pressure tensor measurements.

We also study the difference in the capillary wave spectrum as a function of $\boldsymbol{q}_\perp$ with $\boldsymbol{q}_\perp$ in the plane of the interface, parallel and perpendicular to the director. Typical results are shown in Fig. 18. The low-$q_\perp$ behaviour is roughly consistent with the values of γ deduced from the interface width, and from the earlier pressure tensor calculation. The capillary wave spectrum is anisotropic at higher values of $q_\perp$. Fluctuations parallel to the director are less easy than those perpendicular to the director. The curvature in these figures indicates a *negative* bending rigidity.

8 Colloid Particles in Liquid Crystals

Colloidal particles or droplets suspended in a liquid crystal are of special interest[74]. Elastic deformations of the director field around the colloidal particles produce additional long-range forces between them[75–77]. These interactions can be of dipolar or quadrupolar type depending on the symmetry of the director field around the particles[78], and this in turn is extremely sensitive to the boundary conditions on the particle surface and the size of the particles[79]. The result may be supermolecular structures[74,80], cellular structures[81,82], and even a soft solid[83] can be observed. Colloidal dispersions in liquid crystals also have a wide variety of potential applications[84].

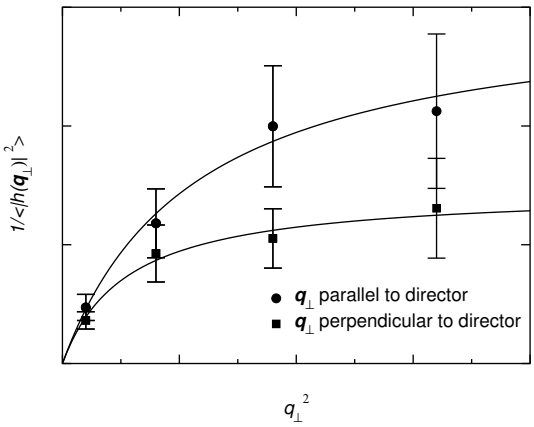

Figure 18. Capillary wave spectrum as function of wavenumber, where the wave vector is directed respectively parallel and perpendicular to the director in the plane of the interface. The lines are to guide the eye (After Ref. 73).

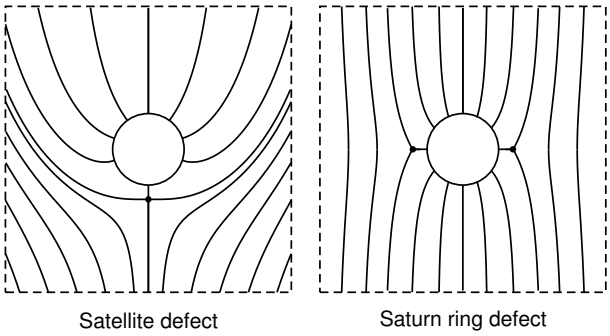

Figure 19. Sketches of director field streamlines around a colloid particle, showing the satellite defect and Saturn ring defect

A key feature here is the presence of *topological defects*[78,85]. Strong homeotropic anchoring of the director, normal to the particle surface, induces a radial hedgehog defect with topological charge $+1$. If the director field is uniform far from the particle, i.e. the total charge of the whole system is zero, topological considerations imply that an additional defect must be created in the medium to compensate the radial hedgehog.

There are several types of defect which can arise in this case. Two are illustrated in Fig. 19. The first is a point defect: a hyperbolic hedgehog with a topological charge -1, called a dipolar or *satellite* defect. The second is a quadrupolar or *Saturn-ring* defect, i.e. a $-1/2$ strength disclination ring that encircles the spherical particle. Theoretical and numerical work based on elastic theory[86,85] suggest that the dipole configuration is stable for the micron-sized droplets which are usually realised experimentally; the Saturn-ring configuration should appear if the droplet size is reduced or an external field is applied[87,88],

and, when present, it is always predicted to be most stable in the equatorial plane normal to the director. The director distortion around the ring defect vanishes with distance in a manner consistent with the *quadrupolar* nature of the defect: far from the particle, at distance r in a direction θ relative to the director, the director deviation angle β has asymptotic behaviour $\beta \sim (R/r)^3 \sin 2\theta$ where R is the particle radius. The director distortion around the satellite defect extends much further than that of the ring defect. This is in accord with its symmetry: far from the particle, the director angle vanishes as $\beta \sim (R/r)^2 \sin \theta$, i.e. it is like a dipolar term in a multipole expansion. To minimize elastic interactions between images in computer simulations, rather larger periodic boxes are required in the satellite defect case.

Earlier investigations have simulated the Saturn ring type of defect for this kind of system[89], using 2048 Gay-Berne ellipsoids. We have recently looked at larger systems[90], investigating the structure for a range of colloid radii R, using soft ellipsoids with elongation $A/B = 3$ for the liquid crystalline solvent. The interaction of each molecule with the droplet was given by a shifted Lennard-Jones repulsion potential between the centers. This results in homeotropic anchoring of the liquid crystal molecules, normal to the particle surface. The systems consisted of 8,000-1,000,000 mesogens.

8.1 Saturn Ring Defect

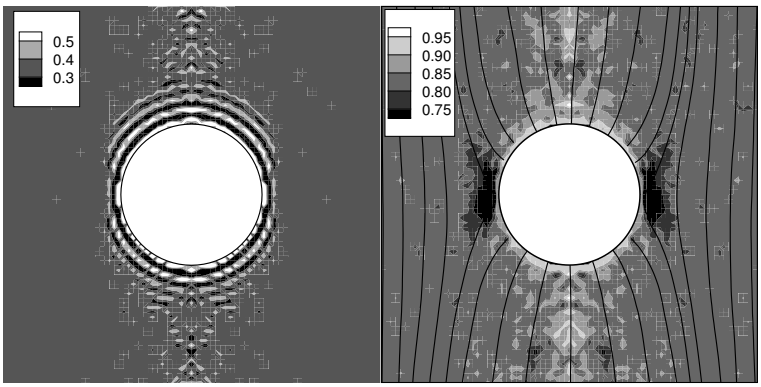

Figure 20. Density map (left) and order parameter map with director streamlines (right) in the spatial region around the colloid particle, for the Saturn ring defect. Droplet radius $R/B = 15$ (After Ref. 90).

For all studied radii in the range $R/B = 3$–15, the ring defect is relatively easy to prepare: it appears immediately after equilibration of the nematic phase of the system starting from the isotropic state, or on enlarging the droplet from a small initial radius in the nematic solvent. It seems likely, therefore, that this type of the defect is energetically more favourable for the chosen droplet sizes.

Typical maps of density and order parameter are shown in Fig. 20. Strong density oscillations can be seen *except* in the region of the defect ring, which is identifiable by greatly reduced orientational ordering. Superimposed on the order parameter map are streamlines of the director field (note that these are not reliably defined in the defect regions

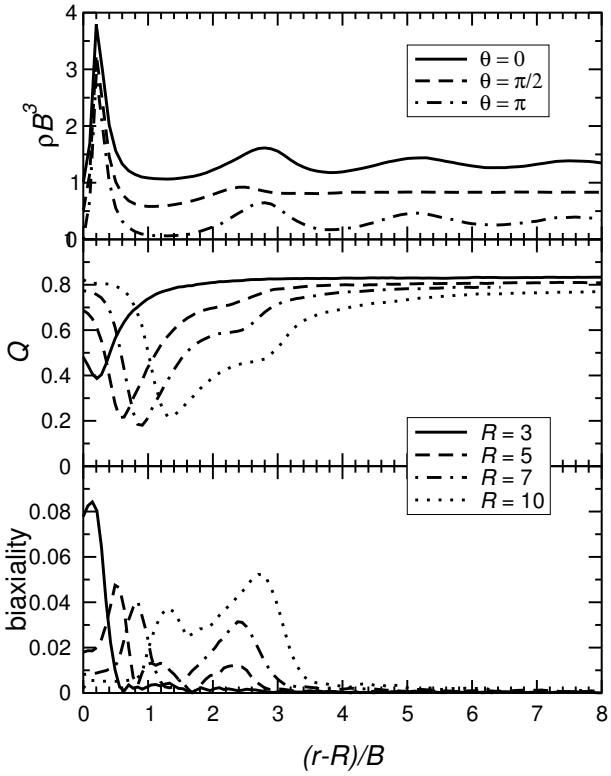

Figure 21. Above: Density profiles for the ring defect. Droplet radius $R/B = 15$, $N = 64000$ particles. The following directions are shown: $\theta = 0, \pi$ (avoiding the defect) and $\theta = \pi/2$ (crossing the disclination ring). Successive curves are offset vertically by 0.5 for clarity. Below: Order parameter and biaxiality profiles for the ring defect along the direction $\theta = \pi/2$. Different curves correspond to the different droplet radii (After Ref. 90).

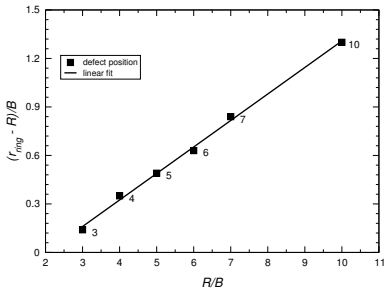

Figure 22. Distance of the core region of the ring defect from the droplet center, as a function of reduced droplet radius R/B. We also show the linear fit to the simulation results, $r_{\text{ring}} = 1.164R - 0.33B$ (After Ref. 90).

themselves, where the order parameter is very low). More detailed information may be obtained by calculating profiles in radial slices. Typical density profiles for the ring defect

with $R/B = 15$ are shown in Fig. 21 for directions $\theta = 0, \pi$ relative to the director (not intersecting the defect) and $\theta = \pi/2$ (crossing the disclination ring). The profiles which avoid the disclination have an oscillating structure near the particle surface which is typical for a *liquid-wall* interface. The profiles which cross the disclination ring do not have oscillations. The difference may be due to the partial melting of the liquid crystal in the disclination core region. This melting damps the influence of the droplet surface on the interface region.

The order parameter and biaxiality profiles for $\theta = \pi/2$ are shown in Fig. 21. The shape of these profiles in general reflects the typical structure of the core: the centre of the core has lower order than the bulk and the core region extends over a few molecular lengths. Both order parameter and biaxiality profiles indicate that the structure of the core is not simple.

Using the minima of the order profiles, we extracted the distance from the core of the disclination ring to the particle surface. The dependence of this distance on the particle radius R is shown in Fig. 22. It is interesting to compare with the phenomenological theory predicting linear dependence of the ring defect radius on the droplet radius: $r_{\text{ring}} \approx 1.25R$ from minimization of the elastic free energy using a trial function[79], $r_{\text{ring}} \approx 1.13R$ using a simulated annealing method[86], or $r_{\text{ring}} \approx 1.26R$[85]. Our MD simulation results give $r_{\text{ring}} - R = -0.33B + (0.164 \pm 0.004)R$ which is in good agreement with the phenomenological theory, especially if one bears in mind the complex structure of the defect core.

8.2 Satellite Defect

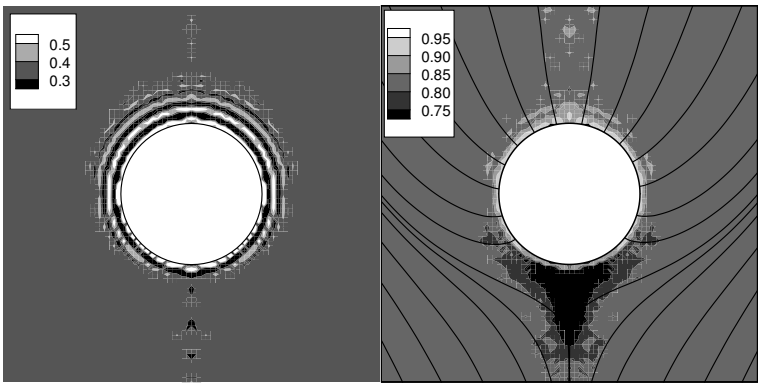

Figure 23. Density maps and order parameter maps with director streamlines for the satellite defect. Droplet radius $R/B = 15$ (After Ref. 90).

To study the satellite defect, one needs very large systems. We used one million particles and droplet radius $R = 15B$. Below this radius, an initial configuration corresponding to the satellite defect structure would transform into the Saturn ring. (For $R = 10B$, this transformation occurred slowly enough to follow; see below).

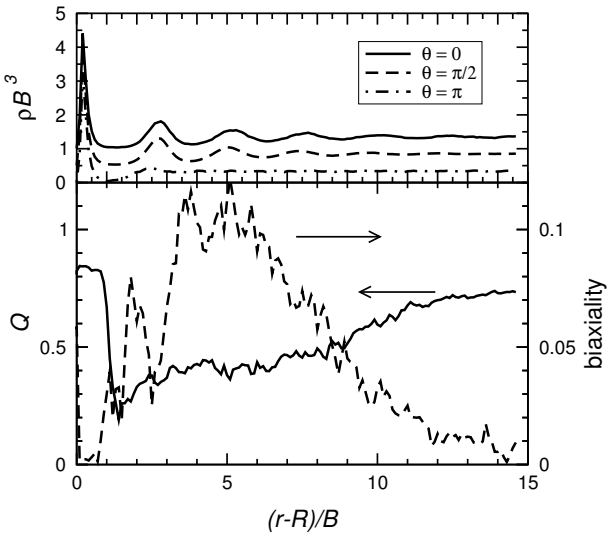

Figure 24. Above: Density profiles for the satellite defect. Droplet radius $R/B = 15$. The following directions are shown: $\theta = 0, \pi/2$ (avoiding the defect) and $\theta = \pi$ (crossing the defect). Successive curves are offset vertically by 0.5 for clarity. Below: Order parameter and biaxiality profiles for the satellite defect along the direction $\theta = \pi$ (After Ref. 90).

Typical maps of density and order parameter are shown in Fig. 23. The density profiles for the satellite defect are shown in Fig. 24. One can see that the density profile at $\theta = \pi$ (across the defect core) has less prominent oscillating structure than the other two: this is again presumably due to the partial disordering of the mesophase in the core region. The order parameter and biaxiality profiles in the $\theta = \pi$ direction are shown in Fig. 24. The defect is rather broad, and difficult to locate from these graphs. However, examination of the director field allows one to place the centre at a distance $r_{\rm sat} \approx 1.4R$. The value predicted by the elastic theory is about $1.22R$ for the simulated annealing calculations[86]; $1.17R$[74] or $1.46R$[91] for the free energy minimization using a trial function.

8.3 Off-Center Ring

Simulation results show that both the satellite and ring defects are at least metastable for $R/B = 15$: once the particular defect is realized in the system, it is stable over the timescale that is accessible to our simulations. However, the satellite defect is not stable for the smaller droplets. Indeed, we observed a rapid transition of the satellite defect to the ring defect for $R/B < 10$. Equilibrating the initial configuration with the satellite defect in the cell with droplet radius $R/B = 10$, we observed that it evolves into an *off-centered* ring defect. The ring then moved slowly, evolving towards an *equatorial* Saturn ring configuration of the usual kind. Doing long runs (up to a million timesteps) we conclude that the off-centred configuration is an intermediate state between the satellite and the Saturn ring defect. The z-coordinate of the ring, relative to the droplet center, as a function of the number of the timesteps, is shown in Fig. 25. The evolution dynamics is quite slow. Note

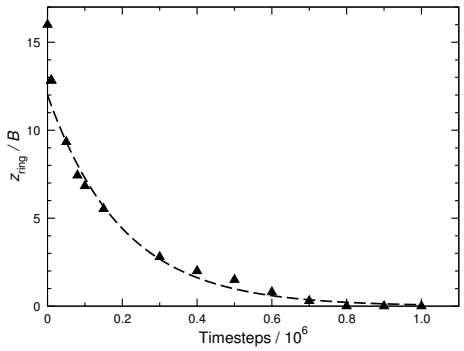

Figure 25. Distance of centre of ring from centre of colloid, as a function of time, for $R/B = 10$ (After Ref. 90).

that elastic theory also predicts the off-center ring configuration to be unstable[85], with the transition from the dipole configuration to the Saturn ring configuration occurring via this intermediate state.

Recently these studies have been extended to measure the solvent-mediated force between two spherical colloids in a liquid crystal[92]. It has been possible to resolve the component of the force perpendicular to the inter-particle vector (which would vanish in an isotropic solvent) and show that it is in qualitative agreement with the predictions of elastic theory. However the component along the inter-particle vector is domainated by solvation structure and depletion effects.

8.4 Non-Spherical Colloidal Particle

For a rod-like elongated particle with length L and transverse size $D \ll L$, and both L and D much greater than the dimensions of the molecules of the liquid crystal, one can have a disclination line of strength -1, a pair of disclination lines of strength $-\frac{1}{2}$, as well as the 'escaped radial' structure, in which the director bends over to become perpendicular to the particle surface[93]. However, from the energetic point of view, the situation is different from the case of the spherical particle. For the elongated particle, both defects are disclination *lines*. The elastic energy per unit length associated with a disclination of strength m is $\pi K m^2 \ln(R/r_0)$, where R is the size of the sample and r_0 is a lower cutoff radius (the core size)[94]. This means that the free energy of a pair of $-\frac{1}{2}$ disclinations is always smaller than that of a single -1 disclination. Therefore, one can expect that the pair of $-\frac{1}{2}$ disclinations will always be a stable configuration, although in principle the -1 defect can still form a metastable state.

Phenomenological (continuum) theory[93] indicates that, depending on the type and strength of anchoring, the equilibrium orientation of the particle $\boldsymbol{s}$ may be either parallel or perpendicular to the liquid crystal director $\boldsymbol{n}$, depending on the ratio of the particle radius to the extrapolation length of the nematic liquid crystal. Qualitatively, the free energy should vary as

$$\mathcal{F} = \mathcal{F}_\perp + \left(\mathcal{F}_\parallel - \mathcal{F}_\perp\right) \cos^2\theta \ , \tag{5}$$

where $\cos\theta = \boldsymbol{n}\cdot\boldsymbol{s}$ and $\mathcal{F}_{\parallel}$ and $\mathcal{F}_{\perp}$ are constants. This gives a $\sin 2\theta$ dependence for the torque and predicts that the director response has a maximum at $\theta = \pi/4$ and is absent at $\theta = 0, \pi/2$. However, it is clear that this description is oversimplified: the defect structure changes while the particle rotates and the nematic ordering evolves in a complicated way.

Molecular dynamics simulations of $N = 64000$ repulsive, soft, ellipsoids of elongation 3 were carried out. For all studied diameters of the rod ($D/B = 5$–20) the -1 strength disclination appears immediately after expanding the colloid particle in the nematic state. However, during the equilibration, it splits into two $-\frac{1}{2}$ disclination lines which then move slowly towards the equatorial plane. We were not able to observe the 'escaped radial' configuration, probably due to the small size of the colloidal particle.

To measure the torque on a rod of finite length, we performed MD simulations in a box with periodic boundary conditions, applying a global constraint for the director along the z axis. An independent measurement was performed in slab geometry, with the walls provided strong homeotropic (along the z axis) anchoring of the director, and with the rod located in the centre of the box. The rod diameter was $D = 5B$, the rod length $L = 10B$. The torque on the rod as a function of tilt angle is presented in Fig. 26. A positive torque tends to align the rod perpendicular to the director. The results presented indicate that the dependence of the torque on the rod tilt angle is far from the $\sin 2\theta$, proposed in[93]; indeed, the torque is not equal to zero for $\theta = 0^\circ$, i.e. there is some symmetry breaking and the orientation of the rod along the director is not even metastable.

For better understanding, a slice in the yz plane is shown in Fig. 26 for different tilt angles of the rod. This shows that the director distribution around the rod is not axially symmetric, and hence the torque is nonzero for $\theta = 0^\circ$. As the rod rotates, the director field becomes less and less frustrated, and finally we have a stable orientation of the rod perpendicular to the director, $\theta = 90^\circ$. In principle, a configuration with axial symmetry is also possible when the rod is along the z axis. However, we were not able to observe it in our simulations even when disordered, isotropic configurations containing the colloidal particle were compressed to the ordered, nematic state.

9 Conclusions

This chapter has attempted to cover several aspects of liquid crystal behaviour that are amenable to study by simulation. It is now possible to tackle features of the structure which have length scales significantly larger than molecular sizes: defects, interfacial fluctuations, distortions due to suspended colloidal particles or droplets. Little mention has been made, due to limitations of space, of many more aspects which are also of great interest: smectic (layered) phases, for instance, or reorientational dynamics and fluid flow, which are important in understanding the operation of liquid crystal devices. These also provide rich fields of study, both by molecular simulation and other modelling techniques, which may extend the accessible length and timescales towards the mesoscopic and macroscopic regimes. Many challenges remain in these areas. Finally, the predictive power of simulations remains limited: it is still quite a challenge to use atomistically correct potentials to predict, reliably, liquid crystalline phase behaviour and properties. Nonetheless, the progress that has been made using simple models is quite encouraging, and the steady increase in available computer power may bring these goals within reach in a few years.

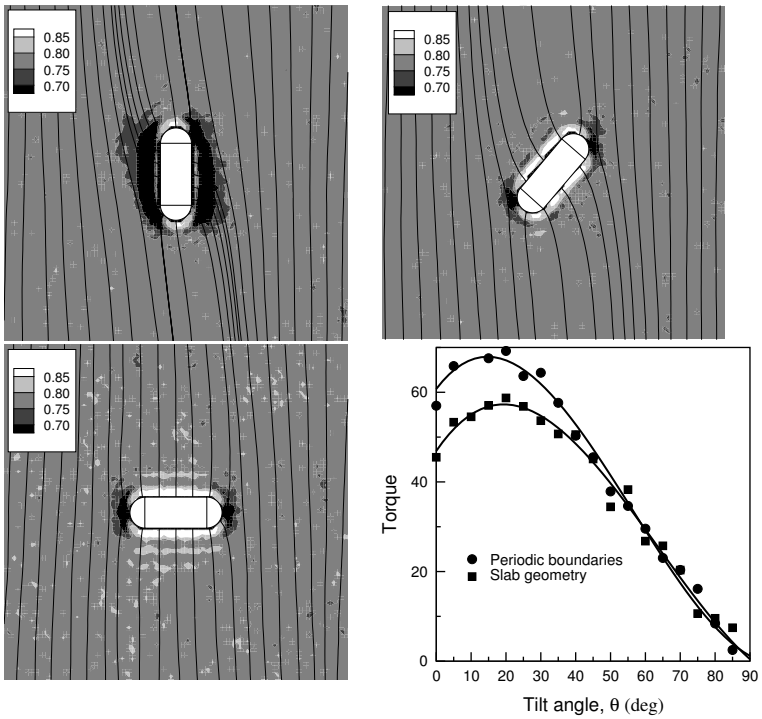

Figure 26. Director streamlines and order parameter maps for different tilt angles. A side view along the x axis is shown (the rod is tilted in the yz plane). We also plot the torque on the rod vs. rod tilt angle for two systems: one with periodic boundaries and the other in slab geometry. The lines are to guide the eye. For more details see Ref. 95

Acknowledgements

It is a pleasure to acknowledge the work of past and present members of my research group, too many to list individually. My work in liquid crystals began with an enjoyable collaboration with Daan Frenkel, and subsequently several members of his group, and was further stimulated by visits to Claudio Zannoni and a period of study leave in Mainz, hosted by Kurt Kremer and Kurt Binder. The support of the Alexander von Humboldt foundation, the British Council ARC programme, the Leverhulme Trust, and the UK Engineering and Physical Sciences Research Council, is gratefully acknowledged.

References

1. M. A. Glaser, R. Malzbender, N. A. Clark, and D. M. Walba. Atomic detail simulation studies of tilted smectics. *J. Phys. Cond. Mat.*, 6:A261–A268, 1994.
2. E. Garcia, M. A. Glaser, N. A. Clark, and D. M. Walba. HFF: a force field for liquid crystal molecules. *J. Molec. Struc. - THEOCHEM*, 464:39–48, 1999.
3. S. J. Clark, C. J. Adam, G. J. Ackland, J. White, and J. Crain. Properties of liquid

crystal molecules from first principles computer simulation. *Liq. Cryst.*, 22:469–475, 1997.
4. S. J. Clark, C. J. Adam, D. J. Cleaver, and J. Crain. Conformational energy landscapes of liquid crystal molecules. *Liq. Cryst.*, 22:477–482, 1997.
5. D. L. Cheung, S. J. Clark, and M. R. Wilson. Parametrization and validation of a force field for liquid-crystal forming molecules. *Phys. Rev. E*, 65:051709, 2002.
6. J. G. Gay and B. J. Berne. Modification of the overlap potential to mimic a linear site-site potential. *J. Chem. Phys.*, 74:3316–3319, 1981.
7. E. de Miguel, L. F. Rull, M. K. Chalam, and K. E. Gubbins. Liquid-vapor coexistence of the Gay-Berne fluid by Gibbs ensemble simulation. *Molec. Phys.*, 71:1223–1231, 1990.
8. R. Berardi, A. P. J. Emerson, and C. Zannoni. Monte Carlo investigations of a Gay-Berne liquid crystal. *J. Chem. Soc. Faraday Trans.*, 89:4069–4078, 1993.
9. E. de Miguel, E. Martín del Río, J. T. Brown, and Michael P. Allen. Effect of the attractive interactions on the phase behavior of the Gay-Berne liquid crystal model. *J. Chem. Phys.*, 105:4234–4249, 1996.
10. J. T. Brown, Michael P. Allen, E. Martín del Río, and E. de Miguel. Effects of elongation on the phase behavior of the Gay-Berne fluid. *Phys. Rev. E*, 57:6685–6699, 1998.
11. R. Berardi, C. Fava, and C. Zannoni. A generalized Gay-Berne intermolecular potential for biaxial particles. *Chem. Phys. Lett.*, 236:462–468, 1995.
12. P. J. Camp and Michael P. Allen. Phase diagram of the hard biaxial ellipsoid fluid. *J. Chem. Phys.*, 106:6681–6688, 1997.
13. P. J. Camp, Michael P. Allen, and A. J. Masters. Theory and computer simulation of bent-core molecules. *J. Chem. Phys.*, 111:9871–9881, 1999.
14. J. S. van Duijneveldt and Michael P. Allen. Computer simulation study of a flexible-rigid-flexible model for liquid crystals. *Molec. Phys.*, 92:855–870, 1997.
15. Alexey V. Lyulin, Muataz S. Al-Barwani, Michael P. Allen, Mark R. Wilson, Igor Neelov, and Nicholas K. Allsopp. Molecular dynamics simulation of main chain liquid crystalline polymers. *Macromolecules*, 31:4626–4634, 1998.
16. J. S. van Duijneveldt, A. Gilvillegas, G. Jackson, and Michael P. Allen. Simulation study of the phase behavior of a primitive model for thermotropic liquid crystals: Rodlike molecules with terminal dipoles and flexible tails. *J. Chem. Phys.*, 112:9092–9104, 2000.
17. R. Berardi, M. Fehervari, and C. Zannoni. A Monte Carlo simulation study of associated liquid crystals. *Molec. Phys.*, 97:1173–1184, 1999.
18. D. Frenkel. Introduction to Monte Carlo methods. In *Computational Soft Matter: From Synthetic Polymers to Proteins*, 2004. this volume.
19. M. P. Allen. Introduction to molecular dynamics simulations. In *Computational Soft Matter: From Synthetic Polymers to Proteins*, 2004. this volume.
20. Michael P. Allen and Dominic J. Tildesley. *Computer simulation of liquids*. Clarendon Press, Oxford, paperback, 385pp edition, 1989.
21. D. Frenkel and B. Smit. *Understanding molecular simulation : from algorithms to applications*. Academic Press, San Diego, 2nd edition, 2002.
22. C. Oseen. Theory of liquid crystals. *Trans. Faraday Soc.*, 29:883–899, 1933.
23. F. C. Frank. On the theory of liquid crystals. *Discuss. Faraday Soc.*, 25:19–28, 1958.

24. G. P. Crawford and S. Žumer. Saddle-splay elasticity in nematic liquid-crystals. *Int. J. Mod. Phys. B*, 9:2469–2514, 1995.
25. G. P. Crawford and S. Žumer, editor. *Liquid crystals in complex geometries formed by polymer and porous networks*, London, 1996. Taylor and Francis.
26. H. Yokoyama. Density-functional theory of surfacelike elasticity of nematic liquid crystals. *Phys. Rev. E*, 55:2938–2957, 1997.
27. P. G. de Gennes and J. Prost. *The Physics of Liquid Crystals*. Clarendon Press, Oxford, second, paperback edition, 1995.
28. L. Onsager. The effects of shape on the interaction of colloidal particles. *Ann. N. Y. Acad. Sci.*, 51:627, 1949.
29. R. Evans. *Adv. Phys.*, 28:143, 1979.
30. R. Evans. Microscopic theories of simple fluids and their interfaces. In J. Charvolin, J. F. Joanny, and J. Zinn-Justin, editors, *Liquids at Interfaces*, pages 1–98, Amsterdam, 1989. Elsevier Science Publishers B.V. Les Houches, Session XLVIII 1988.
31. R. Evans. Density functionals in the theory of nonuniform fluids. In D. Henderson, editor, *Fundamentals of Inhomogeneous Fluids*, chapter 3, pages 85–175. Dekker, New York, 1992.
32. V. V. Ginzburg, M. A. Glaser, and N. A. Clark. Liquid crystal phase diagram of the Gay-Berne fluid by density functional theory. *Liq. Cryst.*, 23:227–234, 1997.
33. J. D. Parsons. *Phys. Rev. A*, 19:1225, 1979.
34. S.-D. Lee. A numerical investigation of nematic ordering based on a simple hard-rod model. *J. Chem. Phys.*, 87:4972–4974, 1987.
35. S.-D. Lee. The Onsager-type theory for nematic ordering of finite-length hard ellipsoids. *J. Chem. Phys.*, 89:7036–7037, 1989.
36. D. Frenkel, B. M. Mulder, and J. P. McTague. Phase diagram of a system of hard ellipsoids. *Phys. Rev. Lett.*, 52:287–290, 1984.
37. D. Frenkel and B. M. Mulder. The hard ellipsoid-of-revolution fluid I. Monte Carlo simulations. *Molec. Phys.*, 55:1171–1192, 1985.
38. R. Evans. Comment. *Molec. Phys.*, 100:199–200, 2002.
39. Philip J. Camp, Carl P. Mason, Michael P. Allen, Anjali A. Khare, and David A. Kofke. The isotropic-nematic transition in uniaxial hard ellipsoid fluids: coexistence data and the approach to the Onsager limit. *J. Chem. Phys.*, 105:2837–2849, 1996.
40. A. Z. Panagiotopoulos. Direct determination of phase coexistence properties of fluids by Monte Carlo simulation in a new ensemble. *Molec. Phys.*, 61:813–826, 1987.
41. A. Z. Panagiotopoulos. Gibbs ensemble techniques. In M. Baus, L. F. Rull, and J.-P. Ryckaert, editors, *Observation, prediction and simulation of phase transitions in complex fluids*, volume 460 of *NATO ASI Series C*, pages 463–501, Dordrecht, 1995. Kluwer Academic Publishers. Proceedings of the NATO Advanced Study Institute on 'Observation, prediction and simulation of phase transitions in complex fluids', Varenna, Italy, July 25–August 5, 1994.
42. I. Nezbeda and J. Kolafa. A new version of the insertion particle method for determining the chemical potential by Monte Carlo simulation. *Molec. Simul.*, 5:391–403, 1991.
43. P. Attard. Simulation of the chemical potential and the cavity free energy of dense hard-sphere fluids. *J. Chem. Phys.*, 98:2225–2231, 1993.
44. D. A. Kofke. Gibbs-Duhem integration: a new method for direct evaluation of phase

coexistence by molecular simulation. *Molec. Phys.*, 78:1331–1336, 1993.
45. Philip J. Camp, Michael P. Allen, Peter G. Bolhuis, and Daan Frenkel. Demixing in hard ellipsoid rod-plate mixtures. *J. Chem. Phys.*, 106:9270–9275, 1997.
46. E. Martín del Río. *Estudio de las propiedades interfaciales de cristales liquidos nematicos*. PhD thesis, Seville University, 1996.
47. Elvira Martín del Río and Enrique de Miguel. Computer simulation study of the free surfaces of a liquid crystal model. *Phys. Rev. E*, 55:2916–2924, 1997.
48. A. P. J. Emerson, S. Faetti, and C. Zannoni. Monte Carlo simulation of the nematic-vapour interface for a Gay-Berne liquid crystal. *Chem. Phys. Lett.*, 271:241–246, 1997.
49. Michael P. Allen. Diffusion coefficient increases with density in hard ellipsoid liquid crystals. *Phys. Rev. Lett.*, 65:2881–2884, 1990.
50. Siegfried Hess, Daan Frenkel, and Michael P. Allen. On the anisotropy of diffusion in nematic liquid crystals: test of a modified affine transformation model via molecular dynamics. *Molec. Phys.*, 74:765–774, 1991.
51. Z. Zhang, O. G. Mouritsen, and M. J. Zuckermann. Weak first-order orientational transition in the Lebwohl-Lasher model for liquid crystals. *Phys. Rev. Lett.*, 69:2803–2806, 1992.
52. Z. Zhang, M. J. Zuckermann, and O. G. Mouritsen. Phase transition and director fluctuations in the 3-dimensional Lebwohl-Lasher model of liquid crystals. *Molec. Phys.*, 80:1195–1221, 1993.
53. Michael P. Allen and Mark A. Warren. Simulation of structure and dynamics near the isotropic-nematic transition. *Phys. Rev. Lett.*, 78:1291–1294, 1997.
54. C. G. Gray and K. E. Gubbins. *Theory of molecular fluids. 1. Fundamentals*. Clarendon Press, Oxford, 1984.
55. M. R. Wilson, Michael P. Allen, M. A. Warren, A. Sauron, and W. Smith. Replicated data and domain decomposition molecular dynamics techniques for simulation of anisotropic potentials. *J. Comput. Chem.*, 18:478–488, 1997.
56. Michael P. Allen, Mark A. Warren, Mark. R. Wilson, Alain Sauron, and William Smith. Molecular dynamics calculation of elastic constants in Gay-Berne nematic liquid crystals. *J. Chem. Phys.*, 105:2850–2858, 1996.
57. E. de Miguel, L. F. Rull, M. K. Chalam, and K. E. Gubbins. Liquid crystal phase diagram of the Gay-Berne fluid. *Molec. Phys.*, 74:405–424, 1991.
58. Michael P. Allen. Molecular simulation and theory of liquid crystal surface anchoring. *Molec. Phys.*, 96:1391–1397, 1999.
59. Michael P. Allen. Modelling liquid crystal structure, phase behaviour and large-scale phenomena. In C. Zannoni and P. Pasini, editors, *Advances in the Computer Simulations of Liquid Crystals*, volume 545 of NATO *ASI Series C*, pages 73–97. Kluwer Academic Publishers, Dordrecht, 2000. Proceedings of the NATO Advanced Study Institute 'Advances in the Computer Simulations of Liquid Crystals', Erice, Italy, June 11-21, 1998.
60. Denis Andrienko, Guido Germano, and Michael P. Allen. Liquid crystal director fluctuations and surface anchoring by molecular simulation. *Phys. Rev. E*, 62:6688–6693, 2000.
61. Denis Andrienko and Michael P. Allen. Theory and simulation of the nematic zenithal anchoring coefficient. *Phys. Rev. E*, 65:021704/1–11, 2002.

62. A. Mertelj and M. Čopič. Dynamic light scattering as a probe of orienational dynamics in confined liquid crystals. *Phys. Rev. E*, 61:1622–1628, 2000.
63. Michael P. Allen. Molecular simulation and theory of the isotropic-nematic interface. *J. Chem. Phys.*, 112:5447–5453, 2000.
64. R. van Roij, M. Dijkstra, and R. Evans. Orientational wetting and capillary nematization of hard-rod fluids. *Europhys. Lett.*, 49:350–356, 2000.
65. R. van Roij, M. Dijkstra, and R. Evans. Interfaces, wetting, and capillary nematization of a hard-rod fluid: theory for the Zwanzig model. *J. Chem. Phys.*, 113:7689–7701, 2000.
66. Muataz S. Al-Barwani and Michael P. Allen. Isotropic-nematic interface of soft spherocylinders. *Phys. Rev. E*, 62:6706–6710, 2000.
67. D. L. Koch and O. G. Harlen. Interfacial tension at the boundary between nematic and isotropic phases of a hard rod solution. *Macromolecules*, 32:219–226, 1999.
68. P. Schofield and J. R. Henderson. Statistical mechanics of inhomogeneous fluids. *Proc. Roy. Soc. Lond. A*, 379:231–246, 1982.
69. A. Harasima. Molecular theory of surface tension. *Adv. Chem. Phys.*, 1:203–237, 1958.
70. J. H. Irving and J. G. Kirkwood. The statistical mechanical theory of transport processes IV The equations of hydrodynamics. *J. Chem. Phys.*, 18:817–829, 1950.
71. Michael P. Allen. Pressure tensor profiles at the isotropic-nematic interface. *Chem. Phys. Lett.*, 331:513–518, 2000.
72. Andrew J. McDonald, Michael P. Allen, and Friederike Schmid. Surface tension of the isotropic-nematic interface. *Phys. Rev. E*, 63:010701(R)/1–4, 2000.
73. Nobuhiko Akino, Friederike Schmid, and Michael P. Allen. Molecular dynamics study of the nematic-isotropic interface. *Phys. Rev. E*, 63:041706/1–6, 2001.
74. P. Poulin, H. Stark, T. C. Lubensky, and D. A. Weitz. Novel colloidal interactions in anisotropic fluids. *Science*, 275:1770–1773, 1997.
75. B. I. Lev and P. M. Tomchuk. Interaction of foreign macrodroplets in a nematic liquid crystal and induced supermolecular structures. *Phys. Rev. E*, 59:591–602, 1999.
76. A. Borštnik, H. Stark, and S. Žumer. Interaction of spherical particles dispersed in a liquid crystal above the nematic-isotropic phase transition. *Phys. Rev. E*, 60:4210–4218, 1999.
77. A. Borštnik, H Stark, and S. Žumer. Temperature-induced flocculation of colloidal particles immersed into the isotropic phase of a nematic liquid crystal. *Phys. Rev. E*, 61:2831–2839, 2000.
78. T. C. Lubensky, D. Pettey, N. Currier, and H. Stark. Topological defects and interactions in nematic emulsions. *Phys. Rev. E*, 57:610–625, 1998.
79. O. V. Kuksenok, R. W. Ruhwandl, S. V. Shiyanovskii, and E. M. Terentjev. Director structure around a colloid particle suspended in a nematic liquid crystal. *Phys. Rev. E*, 54:5198–5203, 1996.
80. P. Poulin and D. A. Weitz. Inverted and multiple nematic emulsions. *Phys. Rev. E*, 57:626–637, 1998.
81. V. J. Anderson, E. M. Terentjev, S. P. Meeker, J. Crain, and W. C. K. Poon. Cellular solid behaviour of liquid crystal colloids: 1. Phase separation and morphology. *Euro. Phys. J. E*, 4:11–20, 2001.
82. V. J. Anderson and E. M. Terentjev. Cellular solid behaviour of liquid crystal colloids:

2. Mechanical properties. *Euro. Phys. J. E*, 4:21–28, 2001.
83. S. P. Meeker, W. C. K. Poon, J. Crain, and E. M. Terentjev. Colloid-liquid-crystal composites: An unusual soft solid. *Phys. Rev. E*, 61:R6083–R6086, 2000.
84. W. B. Russel, D. A. Saville, and W. R. Schowalter. *Colloidal dispersions*. Cambridge University Press, Cambridge, 1989.
85. H. Stark. Director field configurations around a spherical particle in a nematic liquid crystal. *Euro. Phys. J. B*, 10:311–321, 1999.
86. R. W. Ruhwandl and E. M. Terentjev. Monte Carlo simulation of topological defects in the nematic liquid crystal matrix around a spherical colloid particle. *Phys. Rev. E*, 56:5561–5565, 1997.
87. Y. Gu and N. L. Abbott. Observation of saturn-ring defects around solid microspheres in nematic liquid crystals. *Phys. Rev. Lett.*, 85:4719, 2000.
88. J. C. Loudet and P. Poulin. Application of an electric field to colloidal particles suspended in a liquid-crystal solvent. *Phys. Rev. Lett.*, 87:165503, 2001.
89. J. L. Billeter and R. A. Pelcovits. Defect configurations and dynamical behavior in a Gay-Berne nematic emulsion. *Phys. Rev. E*, 62:711–717, 2000.
90. Denis Andrienko, Guido Germano, and Michael P. Allen. Computer simulation of topological defects around a colloidal particle or droplet dispersed in a nematic host. *Phys. Rev. E*, 63:041701/1–8, 2001.
91. S. V. Shiyanovskii and O. V. Kuksenok. Structural transitions in nematic filled with colloid particles. *Mol. Cryst. Liq. Cryst.*, 321:489–500, 1998.
92. M. S. Al-Barwani, G. S. Sutcliffe, and M. P. Allen. Force between colloids in a nematic solvent. submitted.
93. S. V. Burylov and Y. L. Raikher. Orientation of a solid particle embedded in a monodomain nematic liquid crystal. *Phys. Rev. E*, 50:358–367, 1994.
94. M. J. Stephen and J. P Straley. Physics of liquid crystals. *Rev. Mod. Phys.*, 46:617–704, 1974.
95. Denis Andrienko, Michael P. Allen, Gregor Skačej, and Slobodan Žumer. Defect structures and torque on an elongated colloidal particle immersed in a liquid crystal host. *Phys. Rev. E*, 65:041702/1–7, 2002.